Bol. Soc. Paran. Mat.
©SPM – E-ISSN-2175-1188
SPM: www.spm.uem.br/bspm

(3s.) **v. 2026 (44) 7** : 1–25.
ISSN-0037-8712
doi:10.5269/bspm.80773

Thermal and Mass Transport in Maxwell-Boger Nanofluid Flow through a Variable Porous Medium with Endothermic and Exothermic Chemical Reactions

Vinutha Kalleshachar*, Santhosh B. M., Ramesh T. and Sathisha A. B.

ABSTRACT: Riga surface with a variable porous medium plays a vital role in boundary layer flow and flow separation, and its major applications are found in submarines, biomedical, and aircraft. Therefore, the current work examines the impact of activation energy and a variable porous medium via a Riga surface in the existence of Maxwell-Boger nanofluid with endothermic/exothermic chemical reactions, active and passive control of nanoparticles. The similarity transformations are utilized for transforming partial differential equations into dimensionless ordinary differential equations. Additionally, the Runge-Kutta-Fehlberg 4^{th} 5^{th} order and shooting methods are used to resolve the reduced equations, and engineering factors were also examined. Graphical analysis is used to analyse the behaviour of dimensionless factors with their profiles. Notable findings reveal that an increment in activation energy, a drop in temperature in the exothermic, and a rise in the endothermic cases. For increasing values of the porous parameter, velocity profile drops. Streamline patterns and isothermal contours are also illustrated.

Key Words: Nanofluid, Maxwell-Boger fluid, variable porous medium, exothermic/endothermic chemical reaction, activation energy.

Contents

1. Introduction

A base fluid combination of base fluid and only one nanoparticle is named as nanofluid (N-F). N-F initially developed by Choi [1] (1995). The stability of the suspension and heat transport capacities are significantly improved by the suspended nanoparticles in the N-F. Compared to base liquids, N-Fs may improve heat transfer performance. Significant improvements in transfer of heat, flow control, and process efficiency are possible in a variety of industries through the combination of N-F flow with Riga surfaces. It also has many real-world usages in a variety of disciplines, with chemical science, the field of engineering, and biological sciences. N-Fs can also be employed in medical research, automotive electrical work, solar water heating, refrigerators, hybrid-powered engine cooling, thermal exchange machines, increasing diesel generator efficiency, distributing medications, chemical monitoring of neural activity, and tumour removal. The study of N-Fs has recently drawn a lot of interest from current researchers. Using physical factors such as magnetic field, variable thermal conductivity, thermophoresis motion, and Brownian movement in a motion of Sutterby N-F via a stretching sheet including Darcy-Forchheimer porous medium, was scrutinized by Duraihem [2]. Shaheen et al. [3] studied the unsteady characteristics of second-grade N-F circulation across an exponentially curved Riga surface using an artificial neural network. Mandal and Pal [4] probed the motion of a hybrid micropolar N-F via an exponentially shrinking Riga surface in the existence of a porous medium, particularly on entropy optimisation and stability analysis. The influence

* Corresponding author.
2020 *Mathematics Subject Classification:* 76A05.
Submitted December 13, 2025. Published February 22, 2026

of chemical reaction, heat generation/absorbtion, thermophoresis, and Brownian motion on micropolar nanofluid flow through a stretching surface was investigated numerically by Alsulami and Hymavathi [5] using the Galerkin technique. Madhukesh et al. [6] scrutinized Non-newtonian N-F movement via a Riga surface with heat and solutal transmission established by the concentration of pollutant. Li et al. [7] studied the finite difference method on viscous dissipation influenced N-F movements via Riga plates.

Viscosity can differ based on the amount of applied stress in non-Newtonian fluids, i.e., they have a nonlinear relation between shear rate and shear stress. Some of the viscoelastic fluids includes Boger and Maxwell fluids. The characteristic rheological properties and flow behaviour of Maxwell and Boger fluids are very important in fluid mechanics and engineering. The technical and industrial uses of these fluids, including cooling microelectronics, printing, plastic fracturing, crystal development, fibre technology, wire covering, and ceramic materials, have piqued researchers' curiosity. Okasha et al. [8] scrutinised the impacts of local thermal nonequilibrium on the surface tension gradient circulation of a Boger hybrid N-F on a plate using a modified Hamilton-Crosser Model. Vijayalakshmi et al. [9] examined the interesting interaction of radiation, no-slip effects, chemical reactions, and Activation energy (A-E) on the flow dynamics of a Maxwell fluid across a Riga plate. Madhu et al. [10] studied the impacts of A-E, waste discharge concentration, and quadratic heat radiation on the Boger hybrid N-F flow via a stretching cylinder. Ramesh et al. [11] probed the flow, mass, and heat transmission properties of a Maxwell N-F via an extending. Panda et al. [12] probed how heat radiation and various forms of effects affected the thermal properties of Boger-micropolar ternary hybrid N-F magnetised squeezing flow inside parallel concentric discs. A computational study with engineering implications of the thermal-hydrodynamics of a Maxwell fluid with regulated heat and mass transport via a Riga plate was examined by Alrihieli et al. [13].

A variable permeable medium is one of the main impacts in which permeability of the medium changes with respect to the position instead of being constant throughout the material. Variations in structure and compaction in these materials can cause the material's fluid-transmission capacity and the proportion of space to change with position. The transport process in porous materials has been of continuous attention over the last several years. This interest arises from the intricate phenomena associated with transmission processes in porous materials. Due to the wide variety of applications available, several studies have been carried out in this area. Rocks, mud, sponges, and human skin are some examples of porous substances. Numerous investigations into this topic have been prompted by the vast array of applications that are currently accessible. Heat exchangers, thermal energy storage systems, food processing units and recovery of the oil systems are some of the examples of this effect and many researchers are interested in this concept due to their adaptable properties and various applications. In this view, Moreno et al. [14] investigated viscous fluid flow across a porous medium along with variable permeability employing an analytical solution. Tlau and Ontela [15] examined the entropy of hybrid fluid flow via an angled channel in a porous medium with varying permeability while taking isothermal and isoflux conditions into account. Poulikakos and Renken [16] evaluated the consequences of inertia and porosity motion on forced convection along channel. Alnahdi et al. [17] examined the influences of viscous dissipation and radiation on stagnation point movement in a variable permeable surface. Transmission of energy through radiation and heat generation and Darcy law were scrutinized by Tijani et al. [18] for the circulation of a Jeffrey N-F across a movable surface. Tijani et al. [19] investigated the Casson liquid circulation affected by the permeable medium with combination of magnetic field.

A chemical reaction takes place whenever one or more reacting elements transform into a few different substances, forming chemical bonds in the process. The discharge of energy (in the form of heat) outside the surface area (or surrounding) is referred to as an exothermic chemical reaction, and a positive number is used to symbolize this energy. The process of absorbing energy (heat) from the external surrounding area is stated to as an endothermic chemical reaction, which is specified by a negative value. Endothermic and exothermic reactions play a vital role in numerous everyday situations related to chemical reactions, such as food processing (baking, microbial fermentation, and pasteurisation), energy production (power plants), medical science (drug manufacturing), and industrial processes (Haber process). Impact of A-E on the flow of magnetised nanomaterials via Darcy-Forchheimer permeable space with variable features were evaluated by Ullah [20]. The cross-N-F with the impacts of Soret, Dufour, and endothermic/exothermic reactions using a modified Buongiorno tetra-hybrid N-F technique was studied by Sajid

et al. [21]. Madhukesh et al. [22] explored the consequences of endo/exothermic chemical processes on the motion of a N-F via a porous material in a microchannel. Singh et al. [23] inspected the transportation of heat through a cone and wedge using ternary N-F flow with taking exothermic/endothermic processes and A-E into account. Ashrith et al. [24] scrutinized time-dependent N-F motion via a porous stretched surface with bioconvection consequences and endothermic and exothermic reactions. Sajid et al. [25] scrutinized the ternary N-F past via a wedge utilizing a factors, radiation, and endothermic/exothermic processes.

A-E is defined as the least energy need for molecules to experience transformation into a condition that happen a chemical reaction. Arrhenius activation is initially presented by Arrhenius in 1889. A-E is utilised to rise energy conversion and storage gadgets (like fuel cells and batteries), as well as manufacturing operations, including the production of chemicals, oils, and medications. By controlling A-E, scientists create more desirable, efficient, and effective materials, processes, and products. Li et al. [26] scrutinized the bioconvective N-F circulation via an expanding Riga wedge with multiple consequences, such as a heat source, chemical interactions, thermophoresis, and Brownian movement. Rashid et al. [27] probed the bioconvective MHD flow of a fluid via an expanding sheet with A-E and heat radiation. Ali et al. [28] analysed the A-E of a Riga Plate with gyrotactic microorganisms and the creation of entropy through the transmission of mass and heat with heat radiation. Ramasekhar et al. [29] probed the investigation of heat transmission for bioconvection tangent hyperbolic N-F circulation under Riga plate induced by A-E and joule heating. Ali al. [30] examined how the motion of N-F via a nonlinear slender Riga sheet with a viscous dissipation, A-E, thermophoresis, and Brownian motion. Dharmaiah et al. [31] exposed the consequence of A-E and bioconvection N-F circulation over a Riga surface.

Novelty of the study:

The impact of a varivale porous medium of Boger-Maxwell N-F flow across the Riga surface has not been studied, according to the literature review mentioned. In order to fill this study gap in the literature, this study illustrates the mass and heat transmission of Maxwell-Boger N-F flow along a Riga surface, especially with the influence of endothermic/exothermic chemical reactions, and a variable porous medium. A steady, 2-dimensional, incompressible N-F flow via a Riga surface with active and passive control (A-P-C) and A-E is examined in this study. The influences of Titanium oxide (TiO_2) nanoparticles on the thermal performance properties of water (H_2O) N-F flow are examined. The partial differential equations (PDEs) and boundary conditions (BCs) are changed to ordinary differential equations (ODEs), which are then resolved utilizing the Runge-Kutta-Fehlberg 4^{th} 5^{th} order (RKF-45) and shooting method. Additionally, essential engineering coefficients were investigated.

2. Mathematical Modeling and Governing Equations

The following are the assumptions are made in the present study.

1. The flow is in stable, 2-dimensional and incompressible in nature.

2. The variable porous medium is considered in the momentum equation in the presence of Boger-Maxwell nanofluid.

3. The nanofluid is combined with titanium oxide (TiO_2) as a nanoparticles and water (H_2O)as a base fluid.

4. The Riga surface is placed in x direction, and formed by magnets and an electrode. Thus, the existence of the electromagnetic force is taken into consideration for this Riga plate (see **Figure 1**).

5. Wall temperature and wall concentration are symbolized as (T_w, C_w) , respectively. Ambient temperature and ambient concentration are symbolized as (T_∞, C_∞) , respectively.

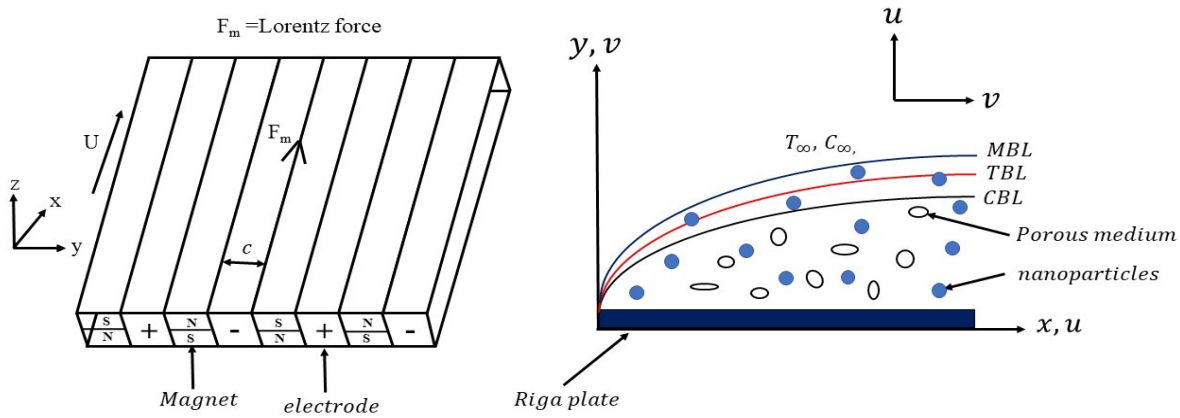

Figure 1: Flow diagram

The main equations for continuity, velocity, conservation of energy, and concentration are discussed below concerning the aforementioned assumptions (see [32], [33], [34], [35], [36])

$$\frac{\partial v}{\partial y} = -\frac{\partial u}{\partial x}, \tag{2.1}$$

$$\begin{aligned} &v\frac{\partial u}{\partial y} + u\frac{\partial u}{\partial x} = \upsilon_{nf}\left(\frac{1+\beta_1}{1+\beta_2}\right)\frac{\partial^2 u}{\partial y^2} - \lambda_0\left(u^2\frac{\partial^2 u}{\partial x^2} + 2uv\frac{\partial^2 u}{\partial x \partial y} + v^2\frac{\partial^2 u}{\partial y^2}\right) + \\ &F_m - \frac{\upsilon_{nf}}{K(y)}u \end{aligned}, \tag{2.2}$$

$$\begin{aligned} &u\frac{\partial T}{\partial x} + v\frac{\partial T}{\partial y} = \alpha_{nf}\frac{\partial^2 T}{\partial y^2} + \frac{\rho_f}{(\rho C_p)_{nf}}\left(\frac{M_{np}}{\rho_{np}}\right)\beta^* k_r^2\left(\frac{T}{T_\infty}\right)^n \exp\left(\frac{-E_a}{KT}\right)(C - C_\infty) + \\ &\tau\left(D_B\left(\frac{M_{np}}{\rho_{np}}\right)\frac{\partial T}{\partial y}\frac{\partial C}{\partial y} + \frac{D_T}{T_\infty}\left(\frac{\partial T}{\partial y}\right)^2\right) \end{aligned}, \tag{2.3}$$

$$v\frac{\partial C}{\partial y} + u\frac{\partial C}{\partial x} - D_B\frac{\partial^2 C}{\partial y^2} = -k_r^2\left(\frac{T}{T_\infty}\right)^n \exp\left(\frac{-E_a}{KT}\right)(C - C_\infty) + \frac{D_T}{T_\infty}\left(\frac{\rho_{np}}{M_{np}}\right)\frac{\partial^2 T}{\partial y^2}, \tag{2.4}$$

The assumed related BCs are as follows (see [35])

$$\left.\begin{aligned} &y = 0 : u = U_w, v = 0, T = T_w, C = C_w\,(active\ control\ of\ \chi)\,, \\ &D_B\left(\frac{M_{np}}{\rho_{np}}\right)\frac{\partial C}{\partial y} + \frac{D_T}{T_\infty}\frac{\partial T}{\partial y} = 0\,(passive\ control\ of\ \chi)\,. \\ &y \to \infty : u = 0, T \to T_\infty, C \to C_\infty. \end{aligned}\right\} \tag{2.5}$$

From equations (2.2-2.5) $F_m\left(= \frac{\pi j_0 M_0}{8\rho_{nf}}\exp\left(-\frac{\pi}{c}y\right)\right)$ represents the electromagnetic force.$j_0, M_0, \& \ c$ represents the applied current density of the electrodes, magnetization of permanent magnets, and the width of the electrodes, respectively. The free stream velocity is portrayed as $U_w\,(= ax)$. Here, (u, v) are the elements of velocity along with the direction (x, y) respectively, υ_f is kinematic viscosity, β_1 is solvent fraction parameter,$\beta_2$is relaxation time ratio, λ_0 is the relaxation time, T is temperature, $\rho_f$is the density of the fluid, $(C_p)_f$is specific heat of the fluid, $M_{np}$is the molar mass of nanoparticles, ρ_{np} is the density of

nanoparticles, β^*, $k_r^2$is the rate of limiting factor for the chemical process, E_a is the A-E, $K$is the Boltzmann constant, C is concentration, D_B is the Brownian diffusion coefficient, D_T is the thermophoretic diffusion coefficient, n is the fitted rate constant, and τ $\left(=\frac{(\rho C_p)_p}{(\rho C_p)_f}\right)$ is the ratio of the heat capacity of the nanoparticle to the fluid heat capacity.
$K(y)=\frac{m^2\delta(y)^3}{(1-\delta(y))^2}$ (see [19]) represents the variable porous medium such that$\delta(y)=\delta_0\left(1+\delta_1\exp\left(\frac{y\delta_2}{m}\right)\right)$. The diameter of the particle is denoted as m, the empirical constant subjected to the diameter of the porous particle is represented as δ_1 & δ_2, and the ambient porosity is represented as δ_0. From [19], one can find that the values of δ_0, δ_1 & δ_2 as 0.5, 0.98, and 1.0, respectively.
The following similarity transformations are used.

$$\left.\begin{array}{l}\eta=\sqrt{\frac{a}{\upsilon_f}}y, v=-\sqrt{a\upsilon_f}f(\eta), u=axf'(\eta), \theta(\eta)=\frac{T-T_\infty}{T_w-T_\infty},\\ \chi(\eta)=\frac{C-C_\infty}{C_w-C_\infty}\,(active\ control), \chi(\eta)=\frac{C-C_\infty}{C_\infty}\,(passive\ control).\end{array}\right\} \tag{2.6}$$

Using (2.6), the governing equations and boundary conditions are transformed into the following form

$$\left.\begin{array}{l}\left(\frac{1}{A_1A_2}\right)\left(\frac{1+\beta_1}{1+\beta_2}\right)f'''-\lambda_1^*\left(-2ff'f''+f^2f'''\right)+\left(\frac{1}{A_2}\right)H_a\exp(-\omega_1\eta)-\\ \left(\frac{1}{A_1A_2}\right)k_1\left(\frac{\left(1-\delta_0\left(1+\delta_1\exp\left(\delta_2\eta\sqrt{k_1}\right)\right)\right)^2}{\left(\delta_0\left(1+\delta_1\exp\left(\delta_2\eta\sqrt{k_1}\right)\right)\right)^3}\right)f'+ff''-f'^2=0\end{array}\right\}, \tag{2.7}$$

$$\left.\begin{array}{l}\left(\frac{k_{nf}}{k_fA_3}\right)\theta''+\left(\frac{1}{A_3}\right)\gamma_1\Pr Cr(1+\Lambda\theta)^n\exp\left(\frac{-E_1}{1+\Lambda\theta}\right)\chi+\\ \Pr\left(Nb\theta'\chi'+Nt\theta'^2\right)+\Pr\theta'f=0\end{array}\right\}, \tag{2.8}$$

$$\chi''-CrSc(1+\Lambda\theta)^n\exp\left(\frac{-E_1}{1+\Lambda\theta}\right)\chi+\left(\frac{Nt}{Nb}\right)\theta''+Sc\chi'f=0. \tag{2.9}$$

The reduced form of BCs is,

$$\left.\begin{array}{l}\eta=0: f'(0)=1, \theta(0)=1, f(0)=0, \chi(0)=1\,(active\ control\ of\ \chi),\\ Nb\chi'+Nt\theta'=0\,(passive\ control\ of\ \chi).\\ \eta\to\infty: f'(\infty)=0, \theta(\infty)\to0, \chi(\infty)\to0.\end{array}\right\} \tag{2.10}$$

Thermophysical properties of N-Fs are (see [7])
Density: $\rho_{nf}=\phi_1\rho_1+(1-\phi_1)\rho_f$.
Dynamic viscosity: $\mu_{nf}=(1-\phi_1)^{-2.5}\mu_f$.
Thermal conductivity: $k_{nf}=\left(\frac{-2\phi_1(k_f-k_1)+k_1+2k_f}{k_1+2k_f+\phi_1(k_f-k_1)}\right)k_f$.
Heat capacity: $(\rho C_p)_{nf}=(\rho C_p)_f(1-\phi_1)+\phi_1(\rho C_p)_1$.
Here, ϕ_1 referred as solid volume fraction. The dimensionless parameters obtained from equations (2.7), (2.8), (2.9), and (2.10) are, Elastic parameter ($\lambda_1^*=\lambda_0 a$), Modified Hartman number $\left(H_a=\frac{\pi j_0M_0}{8\rho_f aU_w}\right)$, Parameter related to the magnitude and width of electrodes $\left(\omega_1=\sqrt{\frac{\pi^2\upsilon_f}{c^2a}}\right)$, Porous parameter $\left(k_1=\frac{\upsilon_f}{m^2a}\right)$, Thermophoresis parameter $\left(Nt=\frac{\tau D_T(T_w-T_\infty)}{T_\infty\upsilon_f}\right)$, Brownian motion parameter $\left(Nb=\frac{\tau D_B(C_w-C_\infty)}{\upsilon_f}\left(\frac{M_{np}}{\rho_{np}}\right)\right)$, Temperature difference parameter $\left(\Lambda_1=\frac{T_w-T_\infty}{T_\infty}\right)$, A-E parameter $\left(E_1=\frac{E_a}{KT_\infty}\right)$, Endothermic/exothermic reaction parameter $\left(\gamma_1=\frac{\beta^*(C_w-C_\infty)M_{np}}{(C_p)_f(T_w-T_\infty)\rho_{np}}\right)$, Prandtl number $\left(\Pr=\frac{(C_p)_f\mu_f}{k_f}\right)$, Chemical reaction parameter $\left(Cr=\frac{k_r^2}{a}\right)$, Schmidt number $\left(Sc=\frac{\upsilon_f}{D_B}\right)$, Local Reynolds number $\left(Re_x=\frac{ax^2}{\upsilon_f}\right)$, and $A_1=(1-\phi_1)^{2.5}$, $A_2=\left(\frac{\rho_1}{\rho_f}\right)\phi_1+(1+\phi_1)$, $A_3=(1-\phi_1)+\frac{(\rho C_p)_1}{(\rho C_p)_f}\phi_1$. **Table 1** provides the thermophysical characteristics of the base fluid and the nanoparticle.
Table 1: Thermophysical characteristics of water and Titanium oxide. (see [32])

Properties	TiO_2	H_2O
Density $(\rho)\left(kgm^{-3}\right)$	4250	997.1
Heat capacity (ρC_p) $\left(Jkg^{-1}K\right)$	686.2	4179
Thermal conductivity (k) $\left(Wm^{-1}K\right)$	8.9538	0.613

Significant engineering coefficients are stated below (see [35], [37])
Nusselt number:

$$\mathrm{Nu} = -\frac{xk_{nf}}{k_f(T_w - T_\infty)} \left.\frac{\partial T}{\partial y}\right|_{y=0}$$

reduced to

$$(\mathrm{Re})^{\frac{-1}{2}} \mathrm{Nu} = -\frac{k_{nf}}{k_f}\theta'(0). \tag{2.11}$$

Sherwood number:

$$\mathrm{Sh} = -\frac{xD_B}{D_B(C_w - C_\infty)} \left.\frac{\partial C}{\partial y}\right|_{y=0}$$

reduced to

$$(\mathrm{Re})^{\frac{-1}{2}} \mathrm{Sh} = -\chi'(0) \ \text{(active control)} \tag{2.12}$$

$$(\mathrm{Re})^{\frac{-1}{2}} \mathrm{Sh} = \frac{\mathrm{Nt}}{\mathrm{Nb}}\theta'(0) \ \text{(passive control)}. \tag{2.13}$$

3. Numerical Procedure

Equations (2.7) – (2.9) and the BCs (2.10) may be solved computationally using the RKF-45 with the Shooting technique. Because of the non-linearity and complexity of these equations, an analytical solution is not attainable. Differential equations of higher order must be changed into 1^{st} order differential equations in order to implement the RKF-45 and Shooting approach. The following are the substitutions:

$$\begin{pmatrix} f, f', f'', \\ \theta, \theta', \theta'', \\ \chi, \chi' \end{pmatrix} = \begin{pmatrix} \varsigma_1, \varsigma_2, \varsigma_3, \\ \varsigma_4, \varsigma_5, D^*, \\ \varsigma_6, \varsigma_7 \end{pmatrix} \tag{3.1}$$

$$f''' = \left(\frac{1}{A_1A_2}\left(\frac{1+\beta_1}{1+\beta_2}\right) - \lambda_1^*\varsigma_1^2\right)^{-1} \begin{pmatrix} -2\lambda_1^*\varsigma_1\varsigma_2\varsigma_3 - \left(\frac{1}{A_2}\right)H_a\exp(-\omega_1\eta) + \left(\frac{1}{A_1A_2}\right)k_1 \\ \left(\frac{\left(1-\delta_0\left(1+\delta_1\exp\left(\delta_2\eta\sqrt{k_1}\right)\right)\right)^2}{\left(\delta_0\left(1+\delta_1\exp\left(\delta_2\eta\sqrt{k_1}\right)\right)\right)^3}\right)\varsigma_2 - \varsigma_1\varsigma_3 + \varsigma_2^2 \end{pmatrix}, \tag{3.2}$$

$$\theta'' = \left(\frac{k_{nf}}{k_fA_3}\right)^{-1} \begin{pmatrix} -\left(\frac{1}{A_3}\right)\gamma_1\,\mathrm{Pr}\,Cr\,(1+\Lambda\varsigma_4)^n\exp\left(\frac{-E_1}{1+\Lambda\varsigma_4}\right)\varsigma_6 - \\ \mathrm{Pr}\left(Nb\varsigma_5\varsigma_7 + Nt\varsigma_5^2\right) - \mathrm{Pr}\,\varsigma_5\varsigma_1 \end{pmatrix}, \tag{3.3}$$

$$\chi'' = CrSc\,(1+\Lambda\varsigma_4)^n\exp\left(\frac{-E_1}{1+\Lambda\varsigma_4}\right)\varsigma_6 - \left(\frac{Nt}{Nb}\right)D^* - Sc\varsigma_7\varsigma_1. \tag{3.4}$$

And the boundary conditions becomes

$$\begin{array}{l} \varsigma_1(0) = 0, \varsigma_2(0) = 1, \varsigma_4(0) = 1, \varsigma_3(0) = \kappa_1, \\ \varsigma_5(0) = \kappa_2. \\ \left.\begin{array}{l} \varsigma_6(0) = 1 \\ \varsigma_7(0) = \kappa_3 \end{array}\right\} active\ control \qquad \left.\begin{array}{l} \varsigma_6(0) = \kappa_3 \\ Nb\varsigma_7(0) + Nt\varsigma_6(0) = 0 \end{array}\right\} passive\ control \end{array} \tag{3.5}$$

Since, the present study we used RKF-45 scheme to obtain the numerical solution and further, shooting procedure is applied to obtain the unknown boundary conditions values stated in equation (3.5). The RKF-45 is used due to its adjustable step size and controlling of error tolerance. The present study we

used 10^{-6} and 0.001 error tolerance and step size respectively. The effective thermophysical properties and their values are utilized during the computation. Additionally, **Table 2** shows the verification of the current study with previous work, and a good match was found.

Table 2: For several values of Prandtl number, valuation of numerical values $-\theta'(\eta)|_{\eta=0}$ with $\beta_1 = \beta_2 = \phi_1 = \lambda_1^* = H_a = k_1 = \gamma_1 = Nb = Nt = Cr = 0$.

Prandtl number	**[38]**	**[39]**	**[40]**	**Current work**
0.72	0.80863135	0.80876122	0.80868	0.80875634
1.0	1.00000000	1.00000000	1.00000	1.00000000
3.0	1.92368259	1.92357431	1.92368	1.92575442
7.0	3.07225021	3.07314679	3.07224	3.07325668
10	3.72067390	3.72055436	3.72067	3.72068235

4. Results and Discussion

The current work investigates the consequence of Boger-Maxwell N-F flow through a Riga surface by considering the impacts of variable porous medium, endothermic and exothermic chemical reaction, and A-E. The analysis further incorporates both A-P-C of nanoparticle mechanisms to study the thermal and mass transmission characteristics. Further, in the present study, we presented both streamlines and isothermal lines with respect to various scenarios.

Figure 2 illustrates the dimensionless $f'(\eta)$for Boger-Maxwell N-F flow along a Riga surface, highlighting the influence and absence of an elastic parameter and the influence of the k_1. In the figure, the solid line denotes the presence of the viscoelastic effect, and dashed lines denote the absence of the viscoelastic effect. The escalation in the values of the $k_1$will decline the $f'(\eta)$ in both the existence and absence of the elastic parameter. It is identified that velocity is less in the case of the presence of an elastic parameter than its absence, indicating that elastic forces present within the fluid will oppose the deformation, reduce the momentum transportation, and decrease the flow. Further, as the $k_1$increases, a further decrease in the $f'(\eta)$ is seen in both cases, indicating that greater resistance occurs due to the k_1.

Practical implications: This influence plays an important role in designing the flow control systems in which porous medium plays a major role, such as oil recovery, targeted drug delivery through various-sized porous tissues.

Figure 3 shows the variation in dimensionless $f'(\eta)$ for several values of modified Hartmann number in the presence and absence of an elastic parameter. It is noted that a rise in the values of the Hartmann number will increase the $f'(\eta)$ in both cases, and further, noticed that the velocity is higher in the absence of the elastic parameter than in its presence. From a physical perspective, the Hartmann number characterizes the impact of the electromagnetic force generated by the Riga surface acts as a flow enhancer. As the values of this parameter rise, the Lorentz force becomes stronger, leading to an improvement in the $f'(\eta)$. When the elastic parameter is present consequently shows the lower velocity due to resistance to deformation introduced by the liquid's viscoelastic nature.

Practical implications: This parameter has crucial applications such as MHD pumps, cooling of electronic equipment, biomedical devices, and propulsion systems.

Figure 4 displays the variation in dimensionless $f'(\eta)$ for various values of the solvent fraction parameter associated with Boger N-F in the presence and absence of the elastic parameter. The velocity upsurges with a rise in the values of the solvent fraction parameter, and observed that the velocity is higher in the absence of the elastic parameter than in its presence. This is due to an escalation in the solvent fraction, which increases the solvent of the fluid and reduces the viscosity and elastic impacts of the N-F which resulting in smoother circulation of the liquid and increasing the $f'(\eta)$. Further, from the figure, it is noticed that velocity is higher in the absence of the elastic parameter than in its presence, which additionally reduces the viscoelastic resistance.

Practical implications: The control of solvent fractions in Boger-type N-Fs allows adjusting the flow rates in systems such as polymer processing, coating applications, N-F-based cooling technologies, and biomedical applications.

Variations in dimensionless $f'(\eta)$ for distinct values of the β_2 in the context of Boger N-F in the presence and absence of an elastic parameter are represented in Figure 5. The escalation in the values of the relaxation time ratio will decrease the velocity in both cases. The velocity is much lower when the elastic parameter is present than in its absence. Physically, an improvement in the scales of relaxation time ratio indicates that the fluid takes a longer time to return to its original state after deformation takes place and intensifies the viscoelastic effects. When an elastic parameter is present, it additionally increases the internal resistance and stress memory within the fluid. Hence, the velocity drops.

Practical implications: The polymer and plastic manufacturing process relies on controlling the flow of viscoelastic materials, where the relaxation time plays a significant role in improving the quality of the product. Fields such as biomedical engineering, oil recovery, thermal management systems, and microfluidics chip technologies will benefit from understanding and optimizing the impacts of relaxation time on the behaviour of the fluid.

Figure 6 displays the changes in dimensionless $\theta(\eta)$for various values of the thermophoresis parameter, considering both endothermic ($\gamma_1 < 0$) and exothermic ($\gamma_1 > 0$) chemical reactions under A-P-C of nanoparticle strategies. It is highlighted that the $\theta(\eta)$ raises with a rise in the values of the thermophoresis parameter in both endo and exothermic chemical reactions and A-P-C cases. This is due to thermophoresis indicates the movement of the particles due to a difference in temperature. An increase in thermophoresis enhances the accumulation of nanoparticles from hotter to colder surfaces, results in the accumulation of heat energy near the surface, and increases the $\theta(\eta)$in both endothermic and exothermic reactions. Further, in the active control, nanoparticles that use external forces exhibit a higher temperature distribution when compared with passive control relies on a natural mechanism to distribute nanoparticles.

Practical implications: These findings are crucial in applications such as thermal therapy in biomedical treatments, electronic cooling systems, solar thermal collectors, chemical reaction chambers, and photothermal conversion equipment.

Figure 7 displays the changes in dimensionless temperature profile for variation in Brownian motion parameter, concerning both endothermic ($\gamma_1 < 0$) and exothermic ($\gamma_1 > 0$) chemical reactions under A-P-C of nanoparticle approaches. Physically, a rise in the Brownian motion parameter (random movement of the particles in the liquid) intensifies the random thermal movement of the nanoparticles, resulting in improved temperature distribution within the liquid. This causes to an improvement in the thermal profile for both kinds of reactions. The temperature distribution is persistently increasing during the exothermic process due to the heat released into the system, hence amplifying the temperature increase induced by Brownian motion. In the endothermic case, heat is absorbed by the system, partially reducing the temperature. Furthermore, the active control of nanoparticles shows a superior thermal profile when compared to the passive control of nanoparticles in maintaining superior thermal conditions.

Practical implications: These results are highly relevant in biomedical applications, chemical reactors, thermal energy storage, microfluidic devices, solar energy systems, and nanocoating processes.

The variation in the dimensionless $\theta(\eta)$for different values of the $Cr$is shown in Figure 8. This analysis considers both endothermic and exothermic reaction cases under the A-P-C of nanoparticles. In the endothermic case, the $\theta(\eta)$ drops, while the exothermic case temperature profile shows reverse behaviour, and in both cases, the active control shows a higher temperature than the passive control. The Crquantitatively measures the rate of thermal energy distribution resulting from a chemical reaction in the N-F. In the exothermic case, a higher chemical reaction releases the additional energy into the liquid and elevates the temperature profile, while in the endothermic case, greater energy is absorbed by the reaction as thermal energy consumed by the surrounding system.

Practical implications: This behaviour is important in catalytic reactors, chemical processing units, biomedical thermal therapies, battery thermal management systems, waste heat recovery systems, and advanced pharmaceutical delivery systems.

The influence of the E_1on the $\theta(\eta)$is indicated in Figure 9. This effect is analysed for both exothermic and endothermic cases under the A-P-C of nanoparticles. From the figure, it is noticed that in the exothermic case, temperature drops, while in the endothermic case reverse behaviour is observed. Physically, A-E denotes the minimum amount of energy essential to initiate the chemical reaction. In the endothermic case, increasing A-E will suppress the rate of reaction and result in reducing the rate of heat absorption

from the N-F, resulting in increased temperature, while in exothermic reactions, elevated A-E reduces the strength of heat-discharging mechanism results in decrease in temperature.

Practical implications: The implications of this phenomenon are crucial in pharmaceutical manufacture, exothermic reactor design, battery and fuel cell technology, nanotechnology catalysts, solar-assisted chemical synthesis, and thermal sensors.

Figure 10 illustrates the influence of the Nton the dimensionless $\chi(\eta)$by considering both active and passive nanoparticle control cases. The increase in the values of thermophoresis will enhance the migration impact from higher to lower temperature regions and leading to a high accumulation of nanoparticles in the cooler region. It is seen that the concentration circulation is significantly higher in the case of active control than passive control of nanoparticles due to external electromagnetic fields. The improved concentration under active control underscores the advantage of controlled nanoparticle transport, perhaps resulting in more uniform and targeted distribution or accumulation.

Practical implications: The outcomes of this impact play a crucial role in drug delivery systems, chemical and biochemical reactors, photothermal energy systems, environmental remediation, and microfluidic diagnosis.

Figure 11 discloses the impact of the Nbon the dimensionless $\chi(\eta)$ concerning A-P-C of nanoparticles. It is viewed that improved values of the Nbwill decrease the concentration in both A-P-C of nanoparticles. It is further observed that passive control of nanoparticles exhibits a higher concentration in comparison to active control of nanoparticles in the presence of the Nb. Physically, as the values of this constraint increase will enhance the random movement of the nanoparticles in the fluid and result in a decrease of localized concentration. In active control of nanoparticles, utilizing external forces, nanoparticles are manipulated in a more controlled way, promoting uniform dispersion rather than clustering of nanoparticles, while in passive control depends on spontaneous Brownian diffusion, leading to a comparative increase in the concentration.

Practical implications: The outcomes of this effect play a significant role in targeted drug delivery systems, N-F-based cooling systems, chemical and catalytic reactors, microfluidic diagnostic devices, and environmental filtration and sensing applications.

The changes in the $\chi(\eta)$for distinct values of Crunder A-P-C of nanoparticles are illustrated in Figure 12. The $\chi(\eta)$diminishes with an upsurge in the values of the Crin both A-P-C cases. This is due to a rise in the values of Cr, and the rate of consumption of nanoparticles is intensified. Active control uses a precise distribution of nanoparticles, and passive control offers limited capacity to resist the deflection effects. Hence, more concentration is in the active case than in the passive case.

Practical implications: The outcomes of this impact are useful in nanocatalysis, chemical reactors, additive manufacturing, energy storage systems, food processing, and preservation.

Figure 13 is presented to show the variations in the dimensionless $\chi(\eta)$due to changes in the $E_1$for A-P-C of nanoparticles. It is seen from the figure that a rise in the values of the E_1 will increase the $\chi(\eta)$in both A-P-C. Further, it is seen that the concentration is higher in the active control case than in the passive control case. As the values of E_1increase, the reaction rate slows down. This results in less consumption of nanoparticles and increases the concentration.

Practical implications: The observed outcomes play a significant role in photocatalysis, production of hydrogen, controlled crystallization and nanomanufacturing, anti-corrosion systems, bio-imaging, and food sensors.

Figures 14 and 15 show the variation of Nuconcerning to E_1 for different values of $Cr$for both active control and passive control of nanoparticles. The results are further analysed for both exothermic and endothermic cases. The rise in the chemical reaction values will significantly decrease the rate of heat distribution due to the change in A-E in both A-P-C cases. It is also observed in both cases that the rate of temperature transmission is higher in the endothermic chemical reaction case than exothermic chemical reaction case due to the release of heat. From a physical point of view, an increase in A-E slows down the chemical process, which in turn slows down the pace at which nanoparticles are used up. The lower rate of reaction makes the rate of heat transfer to dropdown and it is observed that passive control offers greater rate of thermal distribution.

Practical implications: The outcomes show that thermal extraction is suitable for passive control case and these applications including thermal cooling systems in computers, devides which regulates the

thermal control and maintenance systems. In the active control case, it is more advantageous for controlled heating, such as biothermal therapies, microreactors, and thermal sensing drug delivery systems.

Figures 16 and 17 show the variation of Shconcerning to E_1 for different values of Crunder active control and passive control of nanoparticles. The analysis is also made for both endothermic and exothermic chemical reactions. It is noticed that in active control of nanoparticles rate of mass transfer rises, while a reverse trend is observed for passive control of nanoparticles. In an active case, external control mechanisms reduce the damping effects of higher A-E by guiding the nanoparticles to response zones. In passive control, the Sh decreases progressively with increased A-E, indicating reduced species dispersion resulting from decreased response rates and delayed mass transfer.

Practical implications: The outcomes of these control mechanisms suggest that passive control is suited for applications such as filtration systems, thermal coatings, and chemical reactors. In the active control case, bioengineering, nanomedicine, and regulation of species concentration are involved.

The streamline plots (See Figures 18-21) are distinctly depicted for elastic parameters and porous parameters. Figures 18 and 19 show the influence of the elastic parameter in its presence and absence. When the elastic parameter is absent, the streamline shows higher fluid mobility and less resistance. When the elastic parameter is present, the streamlines are increasingly compressed and confined closer to the wall, exhibiting the elastic nature of the fluid by introducing restoring forces. In Figures 20 and 21, in the absence of a porous medium, streamlines show denser lustering and higher velocity magnitudes than their present. When a porous medium is present, velocity weakens and shows a decelerating effect, and limits the momentum distribution into the porous medium.

Isothermal lines represent the visual map of how temperature is distributed in the solid or fluid domain. Figures 22 and 23 show the isothermal lines for exothermic and endothermic chemical reaction cases under active control of nanoparticles. The exothermic case shows closely packed isothermals, indicating concentrated heat zones, while the endothermic case exhibits more moderate spacing. In the passive control case (see Figures 24 and 25), the exothermic case shows the uniform heat distribution, while in the endothermic case, tightly clustered patterns are observed.

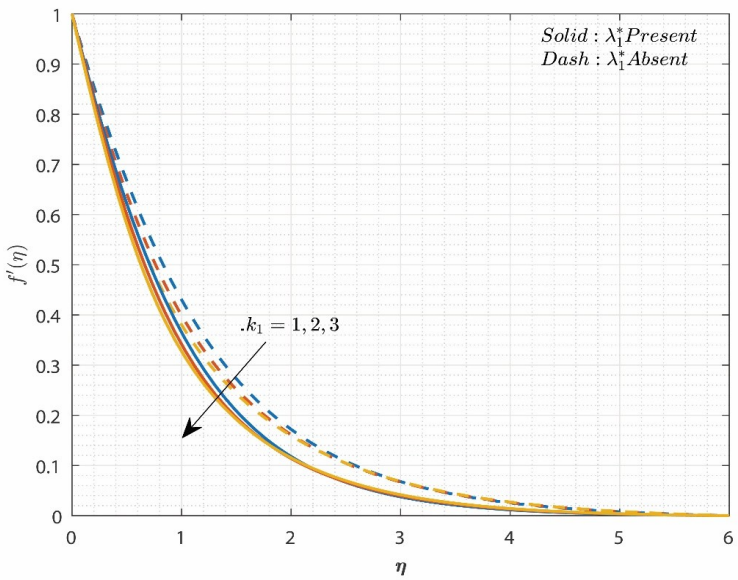

Figure 2: Impact of $k_1$on velocity profile.

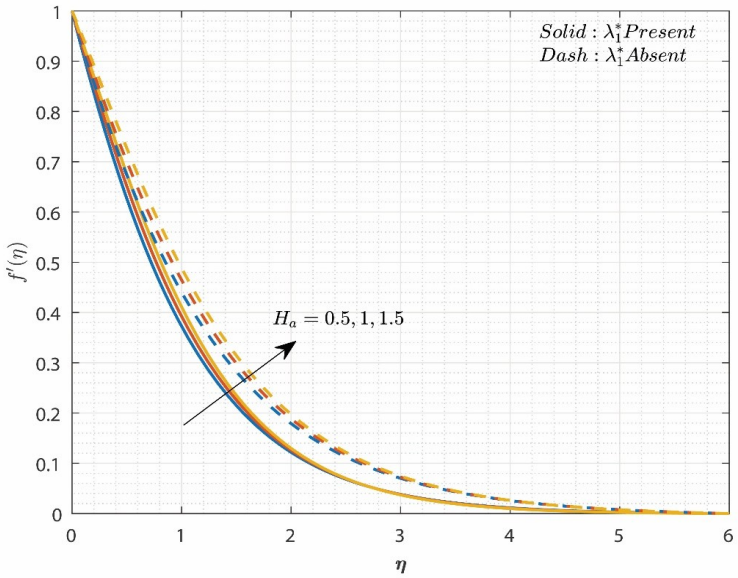

Figure 3: Impact of $H_a$on $f'(\eta)$.

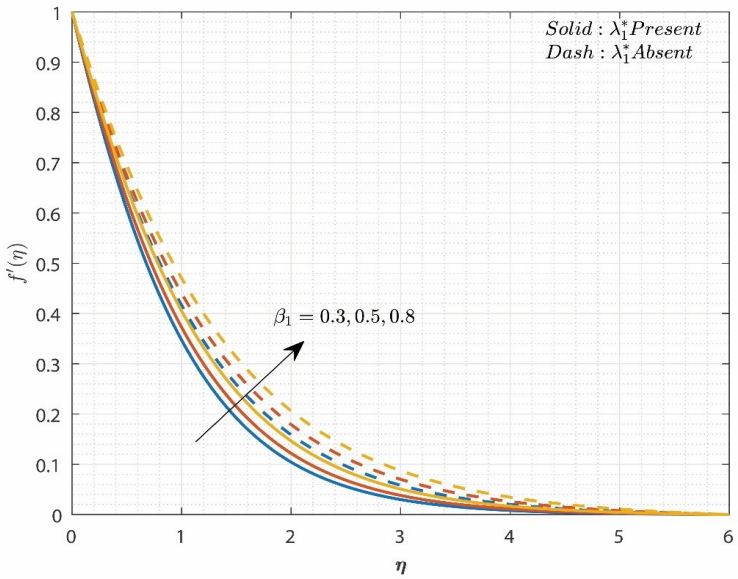

Figure 4: Impact of β_1 on $f'(\eta)$.

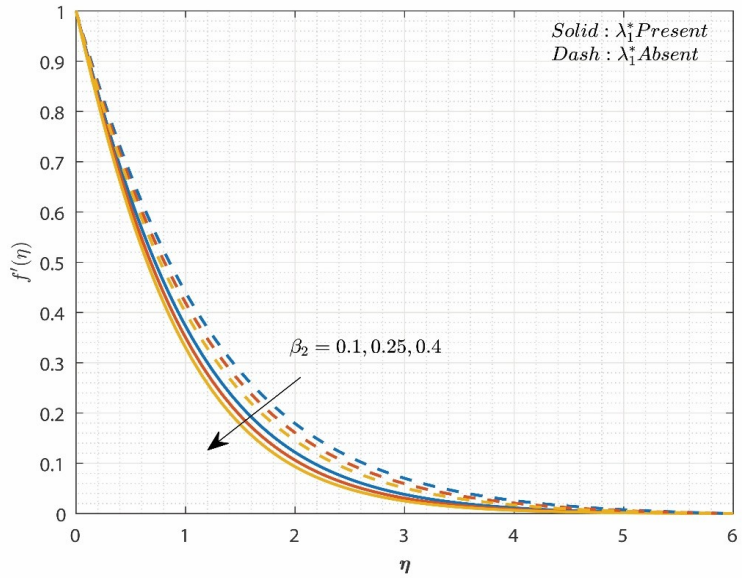

Figure 5: Impact of β_2 on $f'(\eta)$.

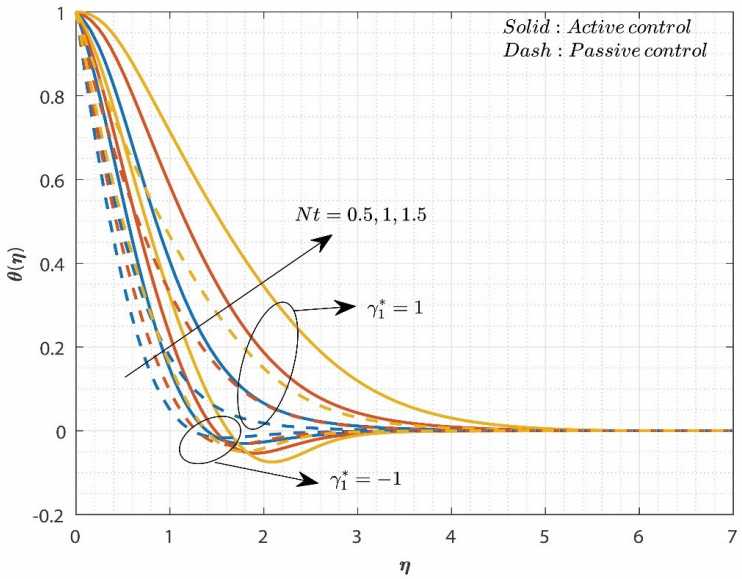

Figure 6: Impact of Nt on $\theta(\eta)$.

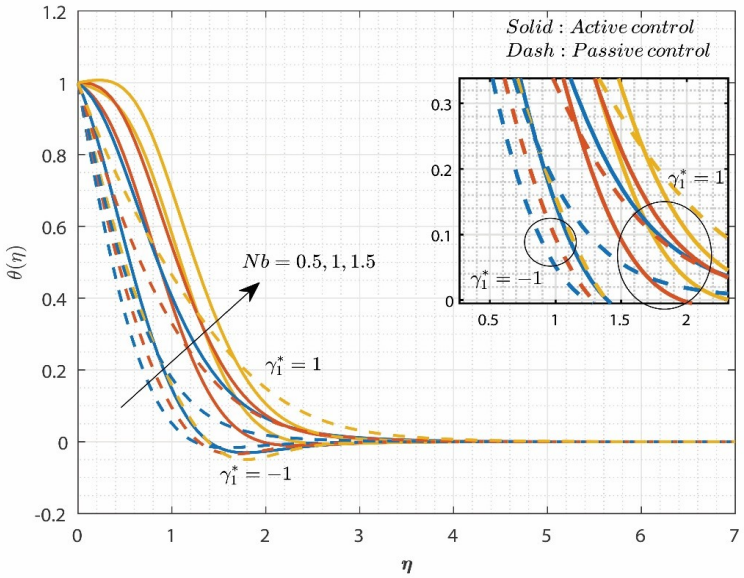

Figure 7: Impact of Nb on $\theta(\eta)$.

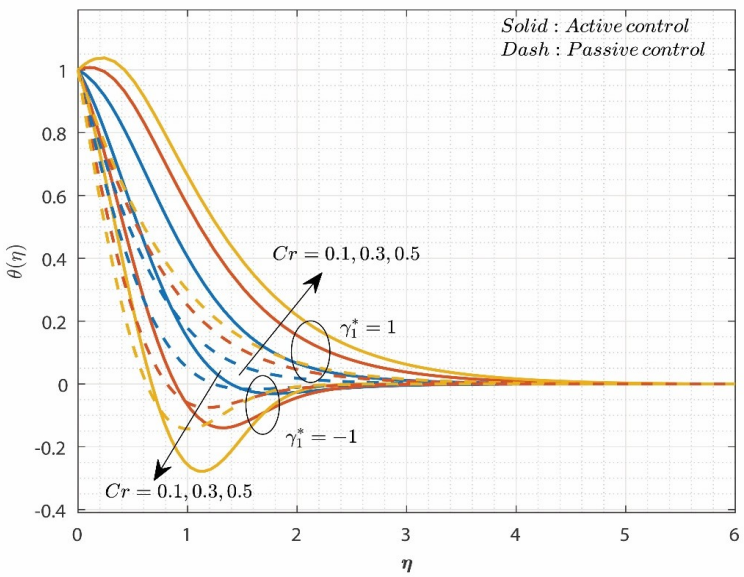

Figure 8: Impact of Cr on $\theta(\eta)$.

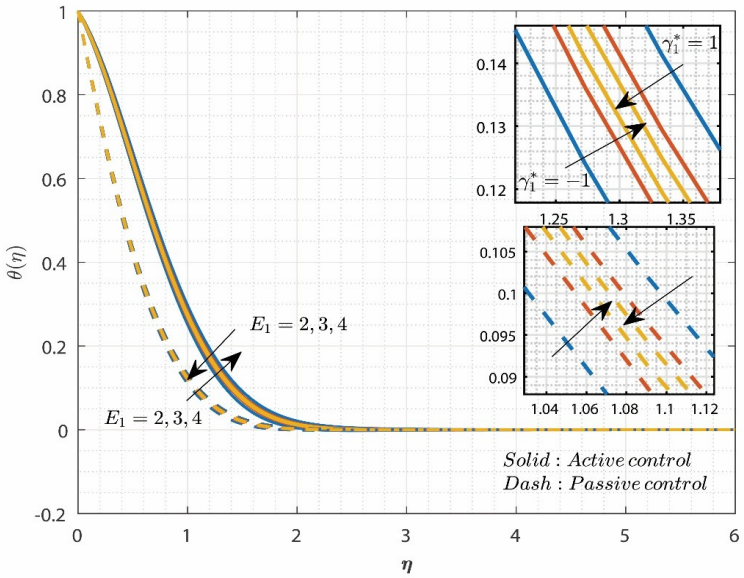

Figure 9: Impact of E_1on $\theta(\eta)$.

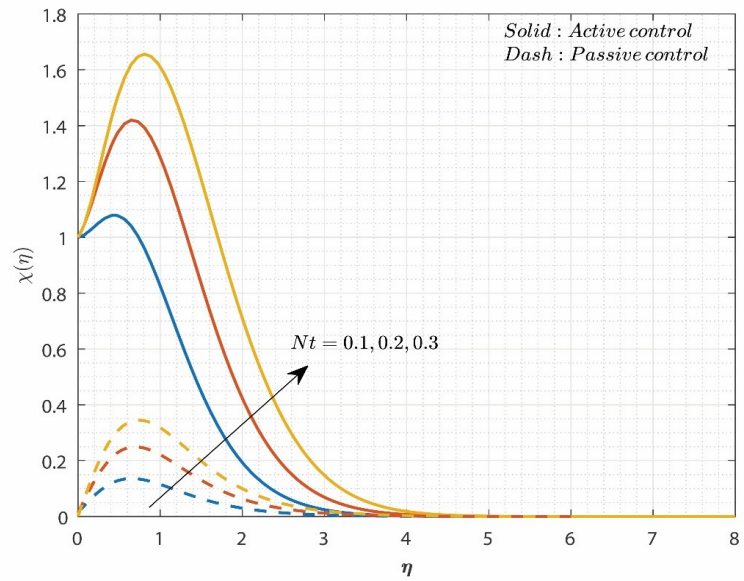

Figure 10: Impact of Nt on $\chi(\eta)$.

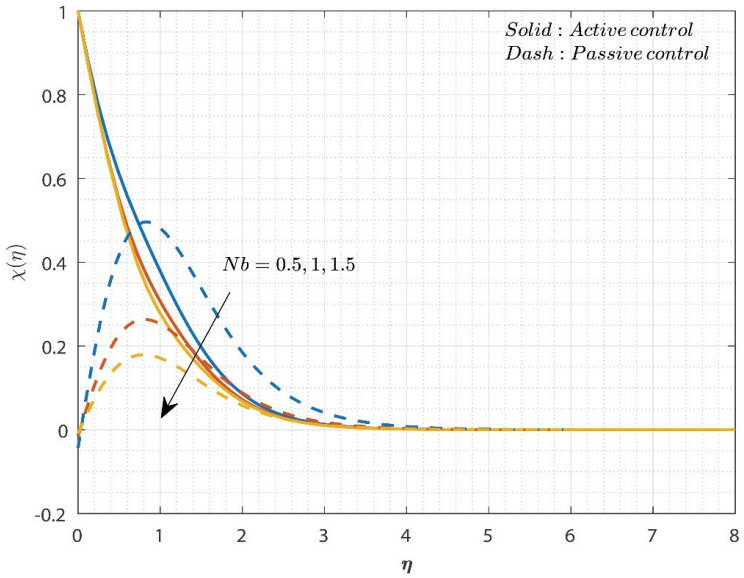

Figure 11: Impact of Nb on $\chi(\eta)$.

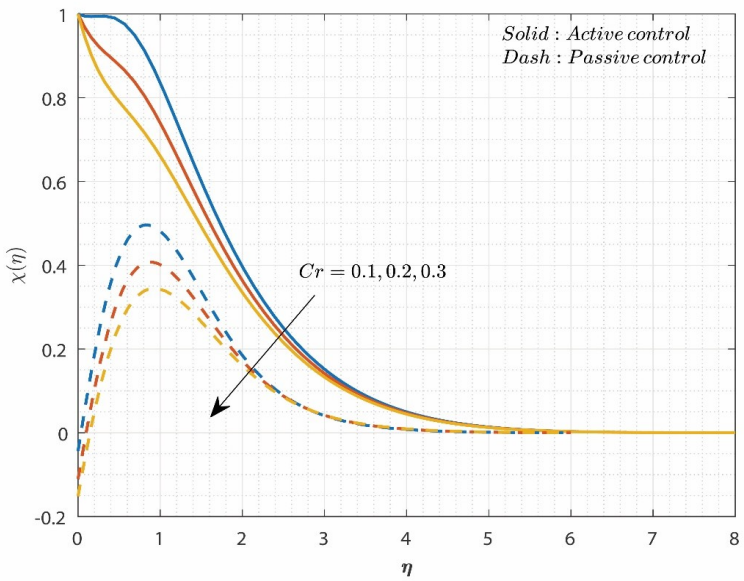

Figure 12: Impact of Cr on $\chi(\eta)$.

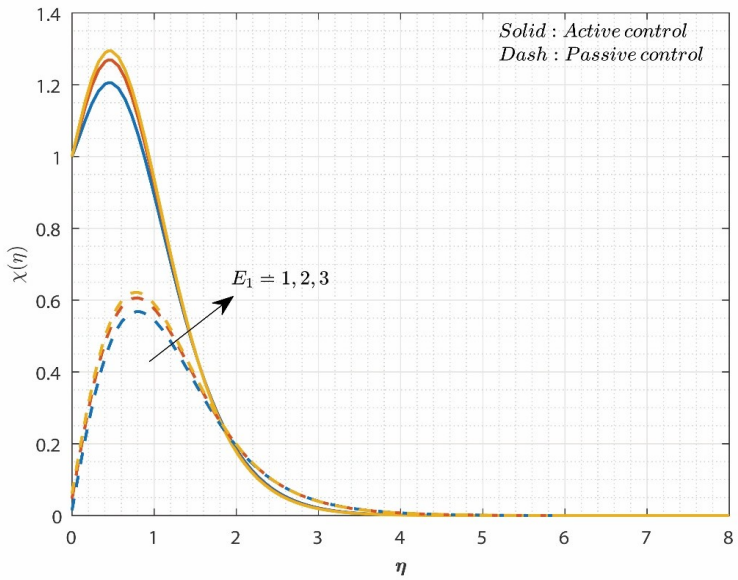

Figure 13: Impact of E_1 on $\chi(\eta)$.

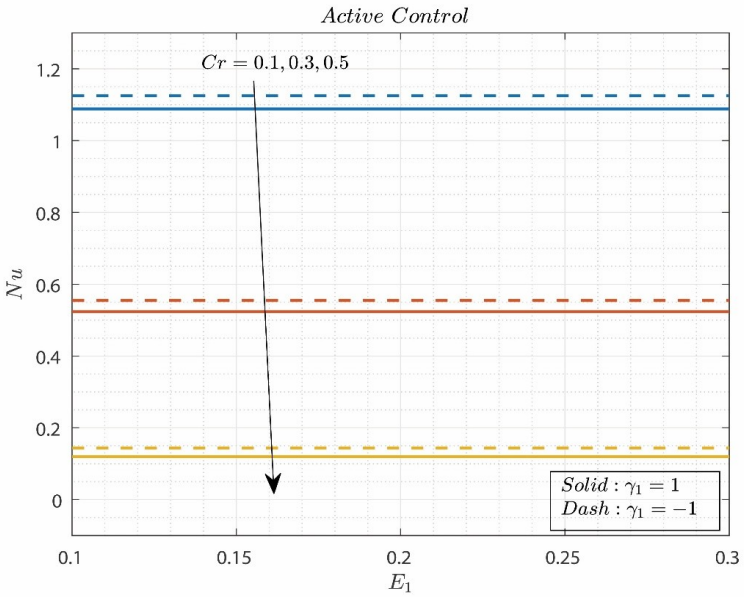

Figure 14: Changes in $Nu$for change in $Cr$and E_1 values (Active control of nanoparticles)

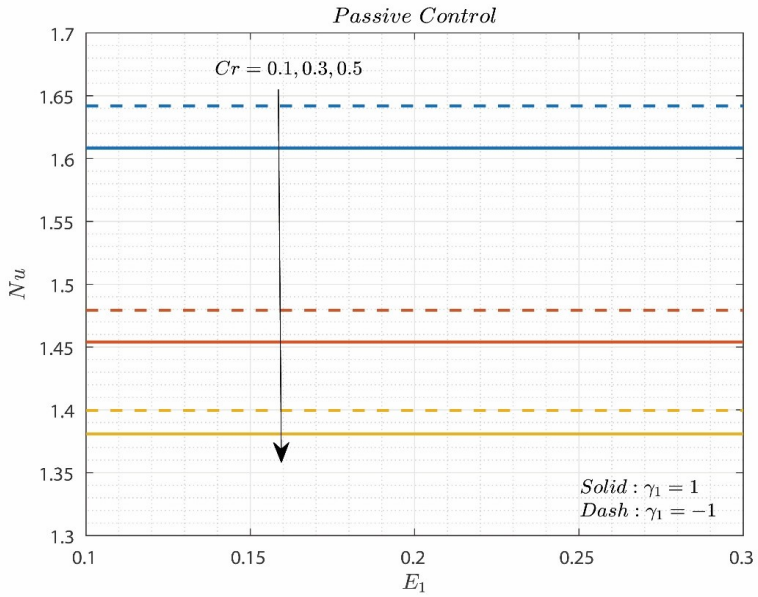

Figure 15: Changes in $Nu$for change in $Cr$and E_1 values (Passive control of nanoparticles)

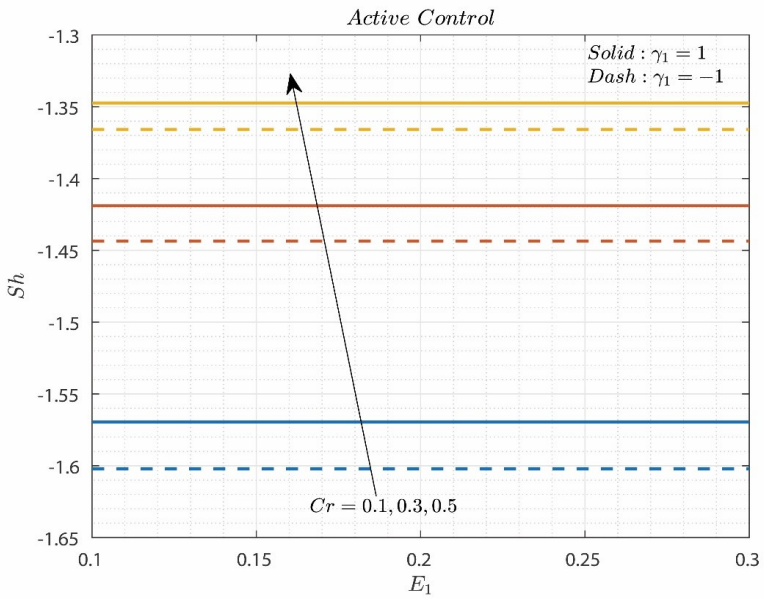

Figure 16: Changes in Sh for change in $Cr$and E_1 values (Active control of nanoparticles).

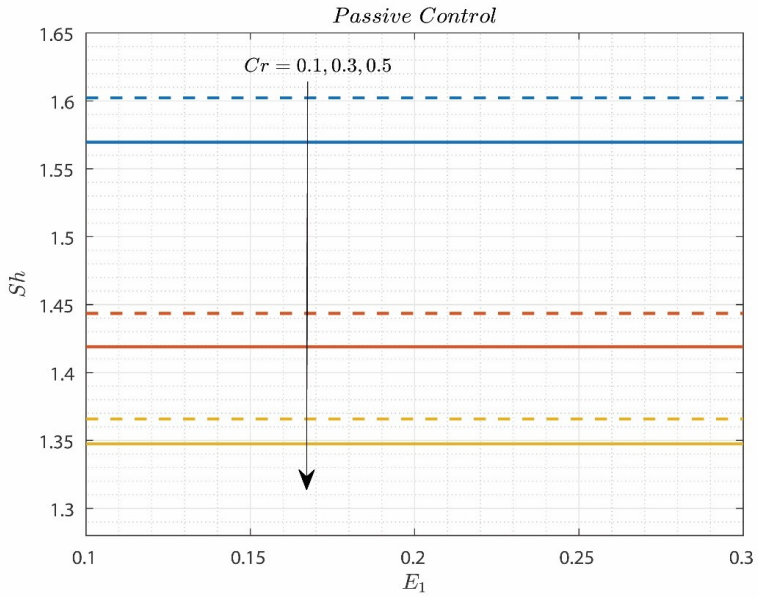

Figure 17: Changes in Sh for change in $Cr$and E_1 values (Passive control of nanoparticles).

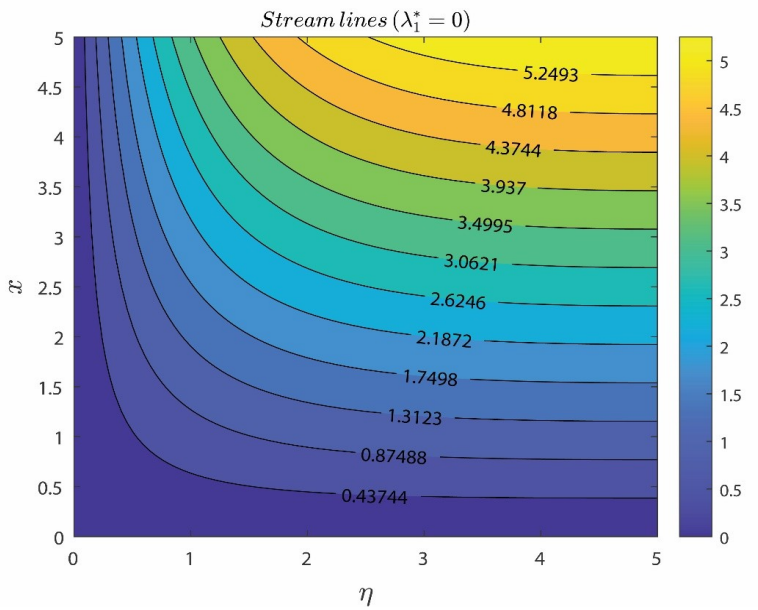

Figure 18: Streamline patterns for $\lambda_1^* = 0$.

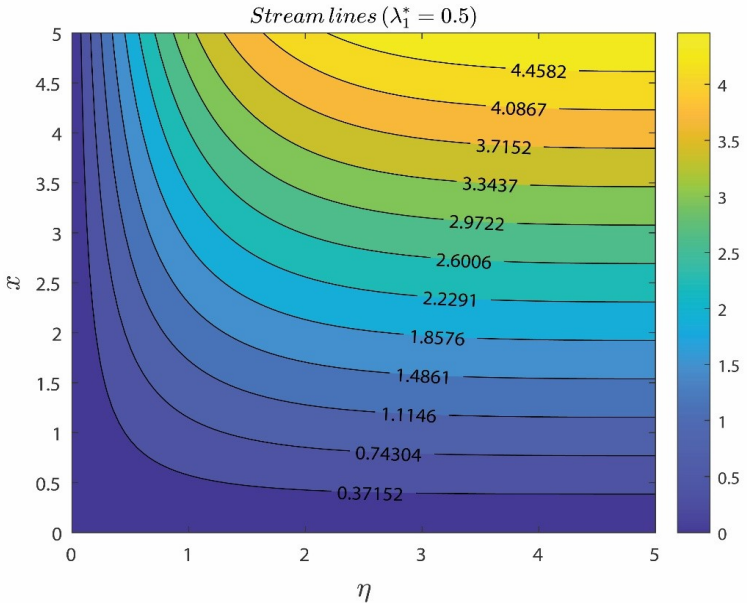

Figure 19: Streamline patterns for $\lambda_1^* = 0.5$.

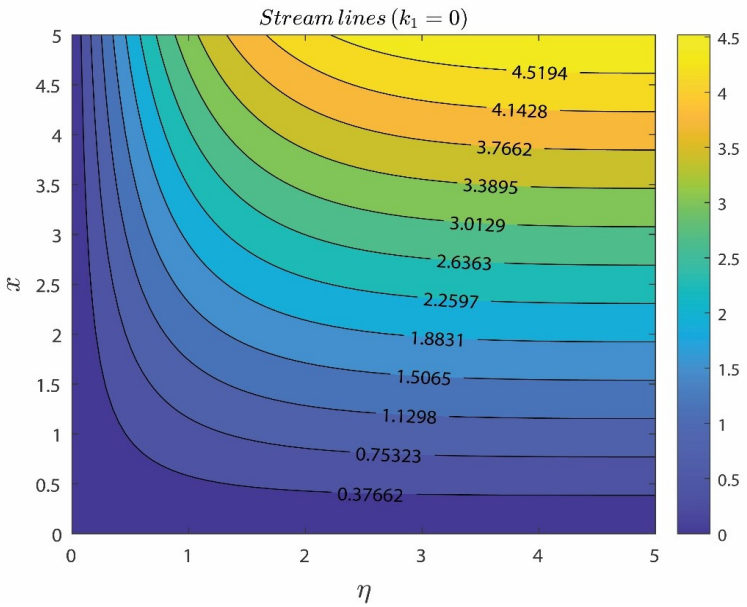

Figure 20: Streamline patterns for $k_1 = 0$.

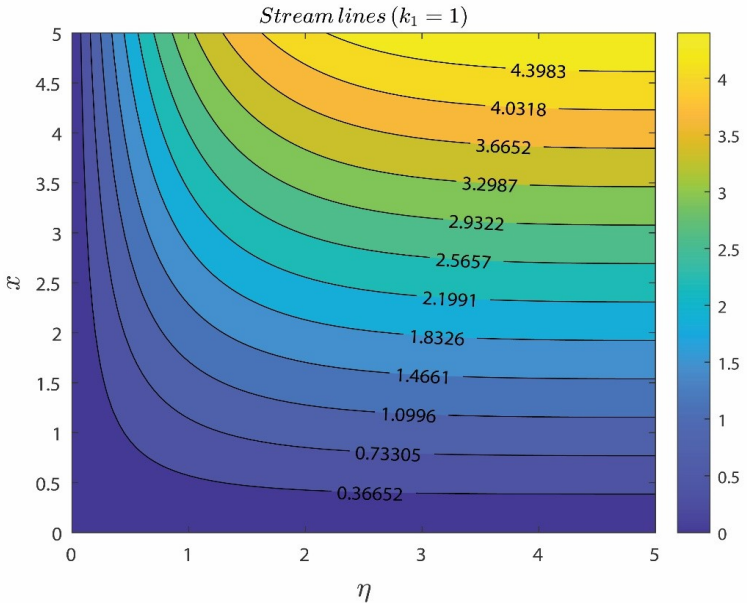

Figure 21: Streamline patterns for $k_1 = 0.5$.

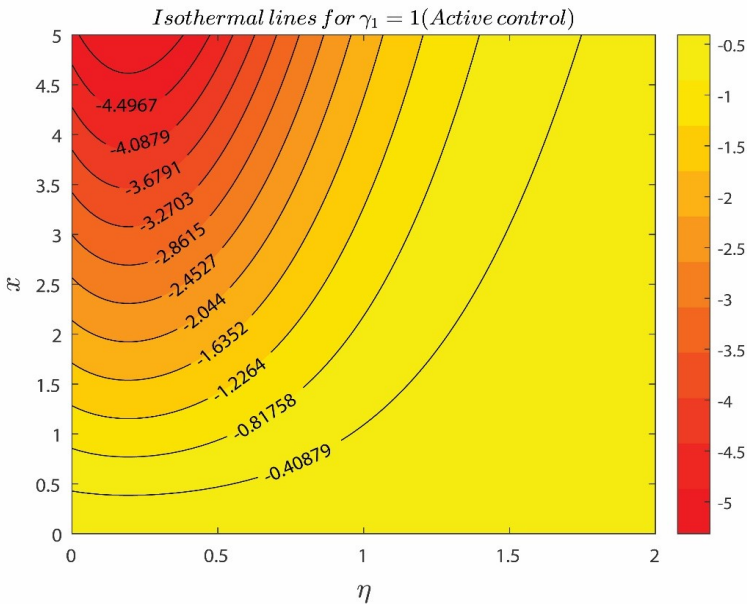

Figure 22: Isothermal lines patterns for Active control of nanoparticles for $\gamma_1 = 1$.

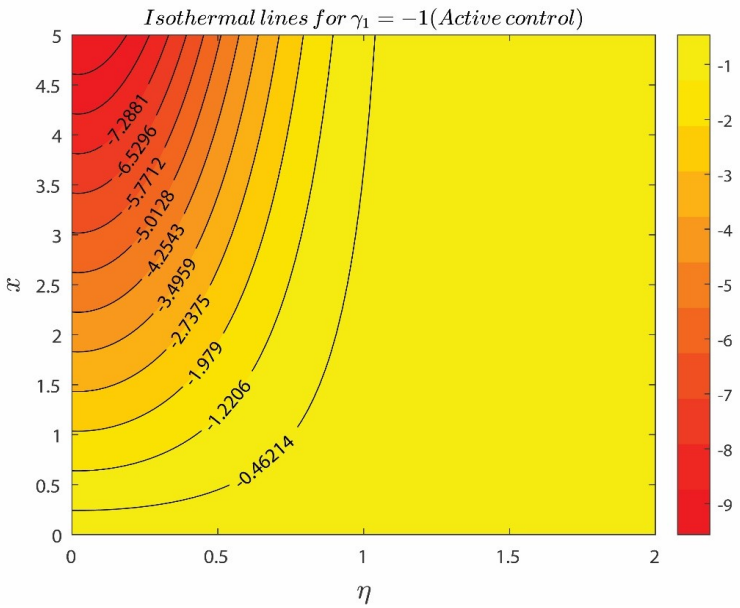

Figure 23: Isothermal lines patterns for Active control of nanoparticles for $\gamma_1 = -1$.

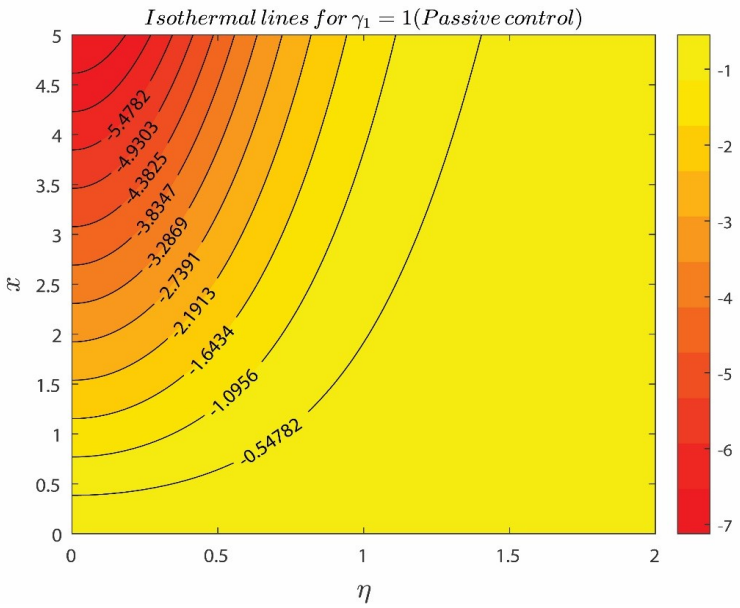

Figure 24: Isothermal lines patterns for the Passive control of nanoparticles for $\gamma_1 = 1$.

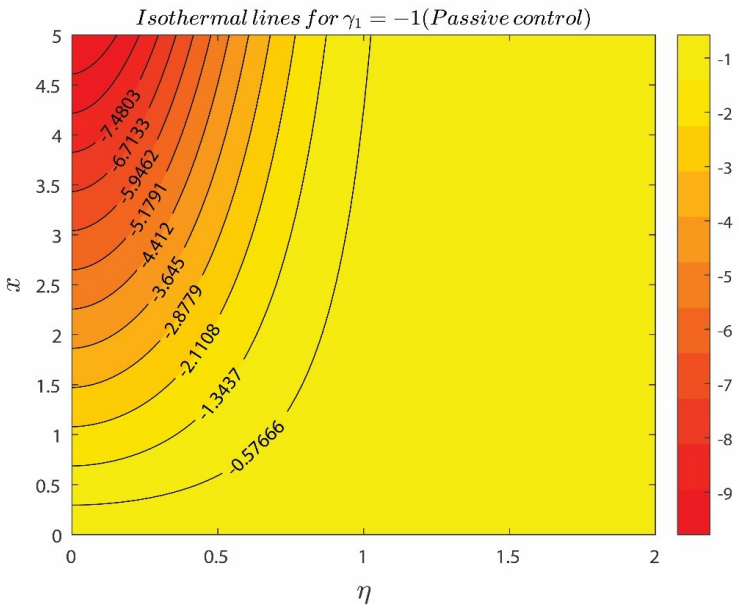

Figure 25: Isothermal lines patterns for the Passive control of nanoparticles for $\gamma_1 = -1$.

5. Conclusion

The current work has examined the mass and energy transmission of a steady, incompressible, two-dimensional, Boger-Maxwell N-F flow via a Riga surface with changing porosity media, A-E, endothermic/exothermic chemical reaction, and active and passive control. The RKF-45 and the shooting approaches are implemented to computationally solve the resulting ODEs and BCs. Graphs are used to analyse the impacts of dimensionless factors on their profiles, including the solvent fraction parameter, relaxation time ratio, modified Hartman number, thermophoresis parameter, A-E parameter, chemical reaction parameter, porous parameter, and Brownian motion parameter. Significant engineering coefficients were also studied to other relevant parameters. For both cases (passive and active control), the isothermal line and streamline patterns were also scrutinized. The significant conclusions of the explorations are summarized below:

1. The velocity profile will decrease when the porous parameter values rise, whether the elastic parameter is present or not.
2. As the values of the solvent fraction parameter get higher, the velocity also rises.
3. The velocity will decrease as the relaxation time ratio values increase.
4. In both situations, the active control shows a greater temperature than the passive control; in the endothermic instance, the temperature profile falls, and in the exothermic scenario, the temperature profile behaves in the opposite way.
5. In both endothermic and exothermic chemical processes, as well as active and passive control scenarios, the thermal profile upsurges as the thermophoresis parameter values increase.
6. The improvement in chemical reaction constraints will result in a drop in the thermal distribution rate due to a change in A-E and observed in active and passive control cases
7. The streamline provides decreased resistance and increased fluid mobility when the elastic parameter is removed. By applying a restoring force, the presence of the elastic parameter causes the streamlines to become more compressed and constricted near the wall.

8. The isothermal visuals exhibit distinct patterns for endothermic and exothermic cases with transitional space lines (endothermic case) and thickly packed lines (exothermic case).

Acknowledgments

Conflict of Interest:
The authors declared no conflict of interest.
Data Availability Statement:
Data will be made available on request.

6. References

1. S. U. S. Choi and J. A. Eastman, Enhancing thermal conductivity of fluids with nanoparticles, Argonne National Laboratory Report ANL/MSD/CP-84938; CONF-951135-29, 1995.

2. F. Z. Duraihem, Electro-magnetohydrodynamic (EMHD) Darcy–Forchheimer flow of Sutterby na nofluid with variable thermal conductivity over a stretching sheet: Finite difference approach, Mod. Phys. Lett. B 39 (2025), 2550019.

3. A. Shaheen, N. Abbas, W. Shatanawi and Z.-e-Huma, Artificial neural network analysis of temperature-dependent properties of second-grade nanofluid flow over an exponentially curved Riga surface, Mod. Phys. Lett. B 2550200 (2025).

4. G. Mandal and D. Pal, Entropy optimization and stability analysis in flow of quadratic radiative Ag–MgO/water hybrid micropolar nanofluid over an exponentially contracting permeable Riga surface, Int. J. Model. Simul. 0 (2025), 1–30.

5. M. D. Alsulami and D. Hymavathi, Melting heat transfer of micropolar nanofluid flow through porous medium, Int. J. Mod. Phys. B 37 (2023), 2350294.

6. J. K. Madhukesh et al., A model development for thermal and solutal transport analysis of non-Newtonian nanofluid flow over a Riga surface driven by a waste discharge concentration, Water 15 (2023), 2879.

7. S. Li et al., Thermodynamic case study of boundary layer viscous nanofluid flow via a Riga surface by means of finite difference method, Case Stud. Therm. Eng. 55 (2024), 104157.

8. M. M. Okasha et al., Characteristics of elastic deformation on Boger hybrid nanofluid using modified Hamilton–Crosser model: A local thermal nonequilibrium model, J. Therm. Anal. Calorim. 150 (2025), 3305–3317.

9. K. Vijayalakshmi et al., Effect of chemical reaction and activation energy on Riga plate embedded in a permeable medium over Maxwell fluid flow, Case Stud. Therm. Eng. 59 (2024), 104457.

10. J. Madhu et al., Influence of waste discharge concentration and quadratic thermal radiation over oblique stagnation point Boger hybrid nanofluid flow across a cylinder, Z. Angew. Math. Mech. 105 (2025), e202300929.

11. P. R. Babu et al., Numerical solutions of steady radiative Maxwell-nanofluid flow toward a stretching sheet in the presence of magnetic field and porous medium, Mod. Phys. Lett. B 39 (2025), 2450432.

12. S. Panda, R. Baithalu and S. R. Mishra, Thermal characteristics of Boger-micropolar tri-hybrid nanofluid magnetized squeezing flow within concentric parallel discs, J. Therm. Anal. Calorim. 149 (2024), 13071–13080.

13. H. Alrihieli et al., Thermal-hydrodynamic analysis of a Maxwell fluid with controlled heat/mass transfer over a Riga plate, Results Eng. 26 (2025), 104801.

14. M. Santos-Moreno, C. V. Valencia-Negrete and G. Fernández-Anaya, Conformable derivatives in viscous flow describing fluid through porous medium with variable permeability, Fractals 30 (2022), 2250178.

15. L. Tlau and S. Ontela, Entropy analysis of hybrid nanofluid flow in a porous medium with variable permeability considering isothermal/isoflux conditions, Chin. J. Phys. 80 (2022), 239–252.

16. D. Poulikakos and K. Renken, Forced convection in a channel filled with porous medium including effects of flow inertia, variable porosity, and Brinkman friction, J. Heat Transfer 109 (1987), 880–888.

17. A. S. Alnahdi et al., Stagnation point nanofluid flow in a variable Darcy space subject to thermal convection using artificial neural network technique, Arab J. Sci. Eng. 49 (2024), 11309–11326.

18. Y. O. Tijani et al., Surface dynamics on Jeffrey nanofluid flow with Coriolis effect and variable Darcy regime, Z. Angew. Math. Mech. 104 (2024), e202300217.

19. Y. O. Tijani, M. T. Akolade and O. Otegbeye, Transport features on bidirectional nanofluid flow with convective heating and variable Darcy regime, J. Comput. Theor. Transp. 52 (2023), 343–362.

20. I. Ullah, Activation energy with exothermic/endothermic reaction and Coriolis force effects on magnetized nanomaterials flow through Darcy–Forchheimer porous space with variable features, Waves Random Complex Media 35 (2025), 398–411.

21. T. Sajid, M. Bilal and G. C. Altamirano, Cattaneo–Christov model for cross nanofluid with Soret and Dufour effects under endothermic/exothermic reactions, ZAMM 105 (2025), e202300044.

22. J. K. Madhukesh et al., Endothermic and exothermic chemical reactions' influences on nanofluid flow across a permeable microchannel with a porous medium, Int. J. Ambient Energy 45 (2024), 2325515.

23. V. Singh et al., Sodium alginate-based MHD ternary nanofluid flow across a cone and wedge with exothermic/endothermic chemical reactions, Numer. Heat Transfer A (2024), 1–20.

24. R. P. Ashrith et al., Sodium alginate-based unsteady nanofluid flow over a porous stretching surface with chemical reaction and bioconvection, Int. J. Ambient Energy 45 (2024), 2404536.

25. T. Sajid et al., Endo/exothermic chemical processes in tri-hybrid nanofluid flow over a wedge with convective boundary and activation energy, Results Phys. 51 (2023), 106676.

26. G. Li et al., Bioconvection for Riga wedge flow of tangent hyperbolic nanofluids with activation energy and mass suction, J. Therm. Anal. Calorim. (2025).

27. A. Rashid et al., Dynamics of bioconvective Walter's-B nanofluid with Cattaneo–Christov heat flux and activation energy, Mod. Phys. Lett. B 38 (2024), 2450330.

28. N. B. Ali et al., Concentration-dependent transport on an unsteady Riga plate including thermal radiation, activation energy and microorganisms, Appl. Rheol. 34 (2024).

29. G. Ramasekhar et al., Heat transfer in bioconvected tangent hyperbolic nanofluid flow with activation energy and Joule heating induced by Riga plate, Case Stud. Therm. Eng. 55 (2024), 104100.

30. B. Ali et al., Electrically conducting mixed convective nanofluid flow past a nonlinearly slender Riga plate with viscous dissipation and activation energy, Mod. Phys. Lett. B 38 (2024), 2450336.

31. G. Dharmaiah et al., Influence of activation energy in steady hydrodynamic non-Newtonian nanofluid with microorganisms, Results Chem. 9 (2024), 101653.

32. S. S. Ghadikolaei et al., Thermophysical properties of TiO2–Cu/H2O hybrid nanofluid dependent on shape factor in MHD stagnation point flow, Powder Technol. 322 (2017), 428–438.

33. M. Abbas et al., Chemical reactive flow of Boger fluid with heat source and local thermal non-equilibrium conditions, Case Stud. Therm. Eng. 59 (2024), 104498.

34. M. Mustafa, J. A. Khan, T. Hayat and A. Alsaedi, Simulations for Maxwell fluid flow past a convectively heated exponentially stretching sheet with nanoparticles, AIP Adv. 5 (2015), 037133.

35. G. K. Ramesh, Active and passive control of nanoparticles in viscoelastic nanomaterial influenced by activation energy and chemical reaction, Physica A 550 (2020), 123964.

36. T. Sajid et al., Endo/exothermic effects in tri-hybrid nanofluid flow over a wedge with convective conditions and activation energy, Results Phys. 51 (2023), 106676.

37. K. Ramesh et al., Bioconvection in Maxwell nanofluid over a Riga surface with nonlinear thermal radiation and activation energy, Surf. Interfaces 21 (2020), 100749.

38. M. H. Abolbashari et al., Entropy analysis for unsteady MHD nanofluid flow past a stretching permeable surface, Powder Technol. 267 (2014), 256–267.

39. S. Das et al., Entropy analysis of unsteady magneto-nanofluid flow past accelerating stretching sheet with convective boundary condition, Appl. Math. Mech. 36 (2015), 1593–1610.

40. A. Mahdy, Unsteady mixed convection boundary layer flow and heat transfer of nanofluids due to stretching sheet, Nucl. Eng. Des. 249 (2012), 248–255.

Vinutha Kalleshachar,
Department of Studies in Mathematics,
Davangere University, Davangere – 577007
INDIA.
E-mail address: vinuthavinu392@gmail.com

and

Santhosh B. M.,
Department of Chemistry,
GM university Davangere-57702
INDIA.
E-mail address: santhoshamma041987@gmail.com

and

Ramesh T.,
Department of Mathematics,
Cambridge Institute of Technology, K R Puram Bengaluru-560036,
INDIA.
E-mail address: ramesh.maths@cambridge.edu.in

and

Sathisha A. B.,
Department of Mathematics,
Government First Grade College, Jagalur, Davanagere, Karnataka
INDIA.
E-mail address: sathishaab@gmail.com